Supporting Information

Remarkable supercapacitor performance of petal-like LDHs vertically grown on graphene/polypyrrole nanoflakes

Dongfeng Du [a], Xiaozhong Wu [b], Shuo Li [a], Yu Zhang [a], Wei Xing [a, *], Li Li [c], Qingzhong Xue [a], Peng Bai [b], Zifeng Yan [b], **

[a] School of Science, State Key Laboratory of Heavy Oil Processing, China University of Petroleum, Qingdao 266580, PR China

[b] School of Chemical Engineering, State Key Laboratory of Heavy Oil Processing, China University of Petroleum, Qingdao 266580, PR China

[c] Australian Institute for Bioengineering and Nanotechnology, The University of Queensland, Brisbane, QLD 4072, Australia

* Corresponding author.

** Corresponding author.

E-mail addresses: xingwei@upc.edu.cn (W. Xing), zfyancat@upc.edu.cn (Z. Yan).

The preparation of GO： Typical, 3 g of natural graphite, 360 mL of H_2SO_4 and 90 mL H_3PO_4 were firstly mixed together in an ice bath. Then 18 g of $KMnO_4$ was slowly added, and the dispersed suspension was transferred to 30 ^oC water bath, followed with vigorous stirring for about 12 h. Finally, 400 mL of ice water and 3 mL of H_2O_2 (30 wt%) was dropped into the solution, turning the colour from dark brown to yellow. The solid product in the suspension was separated and washed with deionized water using high-speed centrifugation at 8000 rpm for 4~5 times until the pH value of the supernatant was neutral. Finally, the sediment was redispersed in deionized water by sonication, giving a homogeneous solution of exfoliated GO (2 mg mL^{-1}).

The preparation of AGP： The black powder GP was firstly mixed with KOH pellets in an agate mortar for 5 mins at mass ratios of 1:2. Then the activation process was performed at 700 ^oC for 2 h with a ramping rate of 5 ^oC min^{-1} under Ar atmosphere. After cooling down to room temperature, the resultant was washed with HCl (10 wt%) and deionized water to remove the residual inorganic salts until the PH value of filtrate became neutral, and finally dried at 120 ^oC for 12 h. The dried product was denoted as AGP.

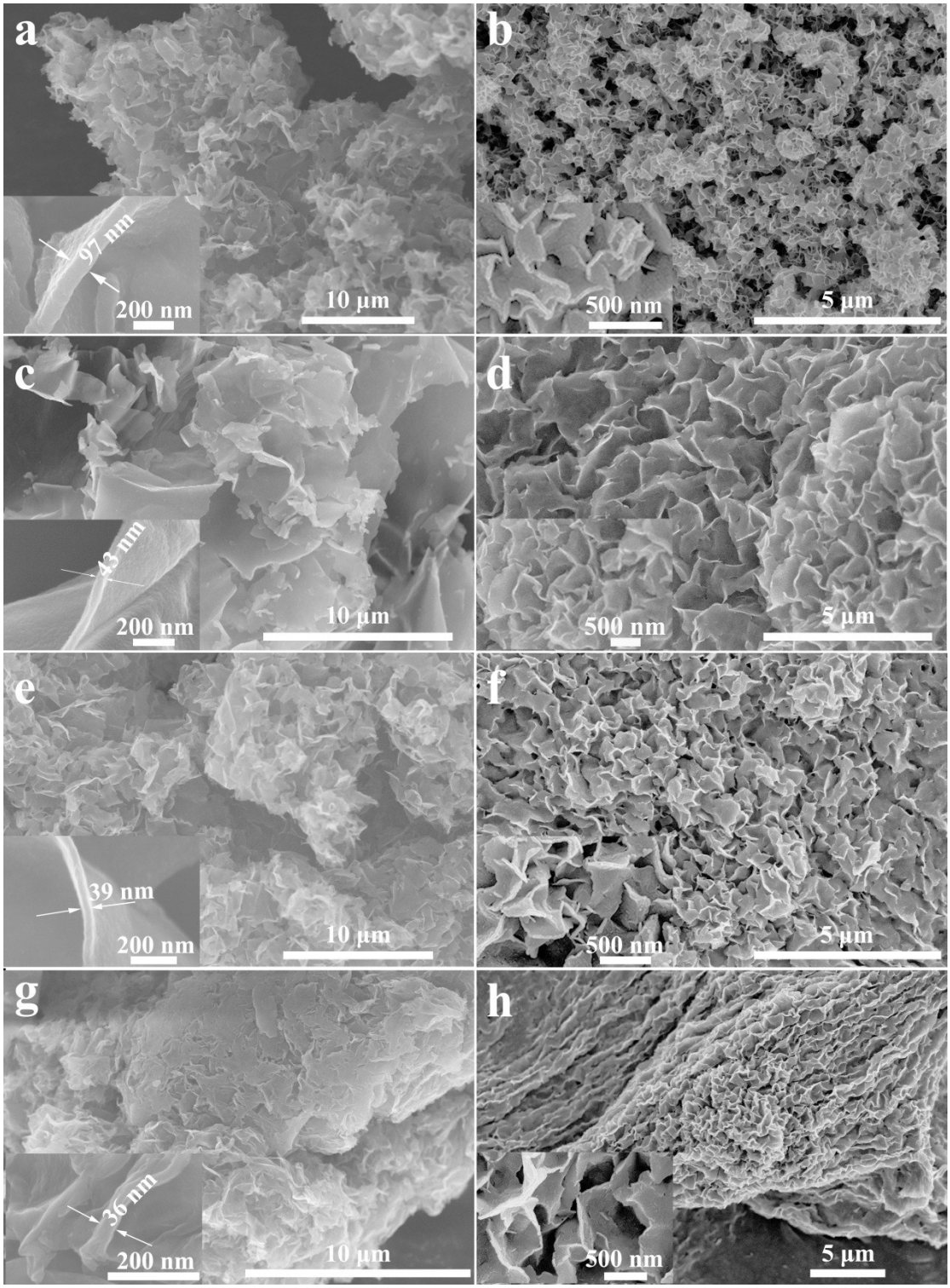

Figure S1. SEM images of GP-1 (a), GP (c), GP-2 (e) and GP-3 (g); and the corresponding GP@LDH-1 (b), GP@LDH (d), GP@LDH (f) and GP@LDH (h).

The thickness of GP-1, GP, GP-2 and GP-3 are 97 nm, 43 nm, 39 nm and 36 nm, respectively (The inset of **Figure S1**). When the GO suspension added is too little, thick

coating of polypyrrole was formed on GO sheets (**Figure S1a**). With the increase of GO suspension added, the thickness of GP could be reduced, but when the 40 mL GO suspension (2 mg mL^{-1}) was added, the as-prepared GP generally shows their morphology of highly curving sheets (**Figure S1g**). Additionally, the corresponding GP@LDH composites exhibited similar morphology when LDHs were coated on the surface of GPs (**Figure S1b, d, f, h**).

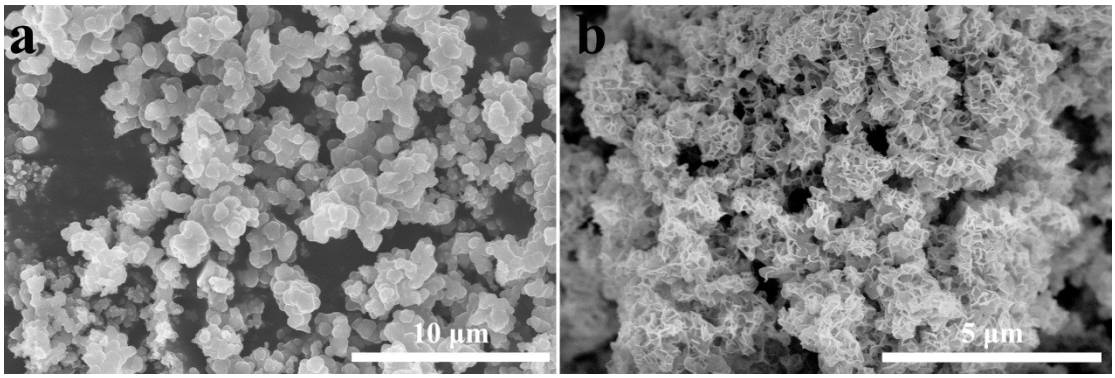

Figure S2. SEM images of PPy (a) and PPy@LDH (b).

We can find that the PPy without GO added tends to form spheres with size of one micron (**Figure S2a**). When the LDHs were coated on the surface of PPy, flower-like PPy@LDH composite was formed (**Figure S2b)**.

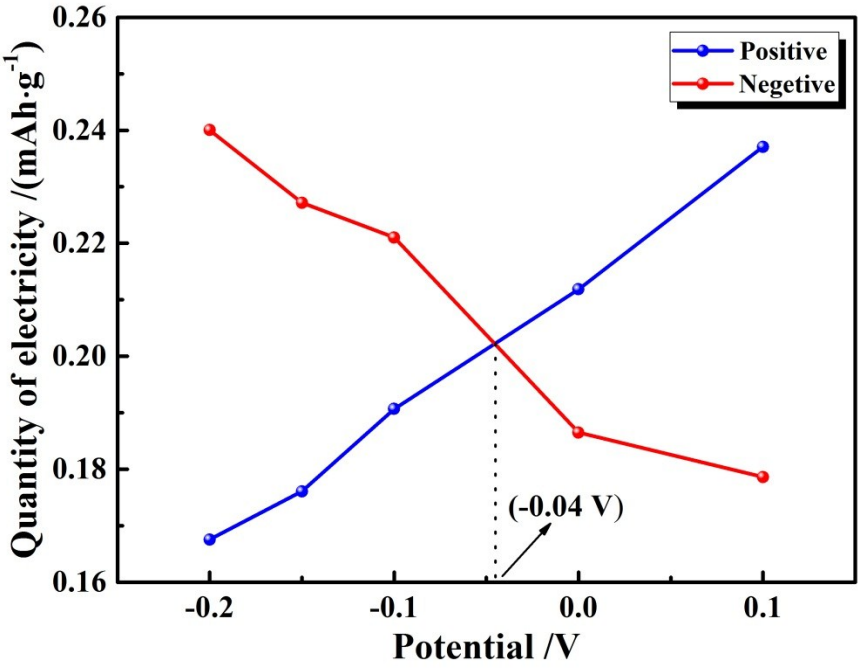

Figure S3. The variation of electric quantity with potential for the electrodes. The positive and negative electrodes are GP@LDH and AGP, respectively. For positive electrode: the discharge capacity from 0.45 V *vs.* SCE to different potentials (0.1, 0, -0.1, -0.15, -0.2 V *vs.* SCE). For negative electrode: the discharge capacity from -1.15 V *vs.* SCE to these potentials (0.1, 0, -0.1, -0.15, -0.2 V *vs.* SCE). When the potential is set to -0.04 V *vs.* SCE, the quantity of the positive and negative electrodes is balanced.

An asymmetric supercapacitor (ASC) denoted as GP@LDH//AGP was assembled using GP@LDH and AGP as the positive and negative electrode materials, respectively. Two half-cells (a platinum film as a counter electrode and a SCE as a reference electrode) were firstly assembled for a series of GCD tests within different potential windows to determine the optimum E_{0V}.[1] One half-cell (comprise positive electrode) was tested between the upper limit potential of 0.45 V vs. SCE and different lower potentials (0.1, 0, -0.1, -0.15, -0.2 V vs. SCE). And the other half-cell (comprise negative electrode) was tested between this series of potentials (0.1, 0, -0.1, -0.15, -0.2

V vs. SCE) and -1.15 V vs. SCE. The potential that makes a balance between the specific capacity of the negative and positive electrodes is taken as the optimum E_{0V} (-0.04 V at this case). Then the half-cells were charged at E_{0V} for 2 h to tune the potentials of both positive and negative electrodes using electrochemical charge injection (ECI) method.[1] Finally, the two electrodes with tuned potentials were assembled into an ASC device.

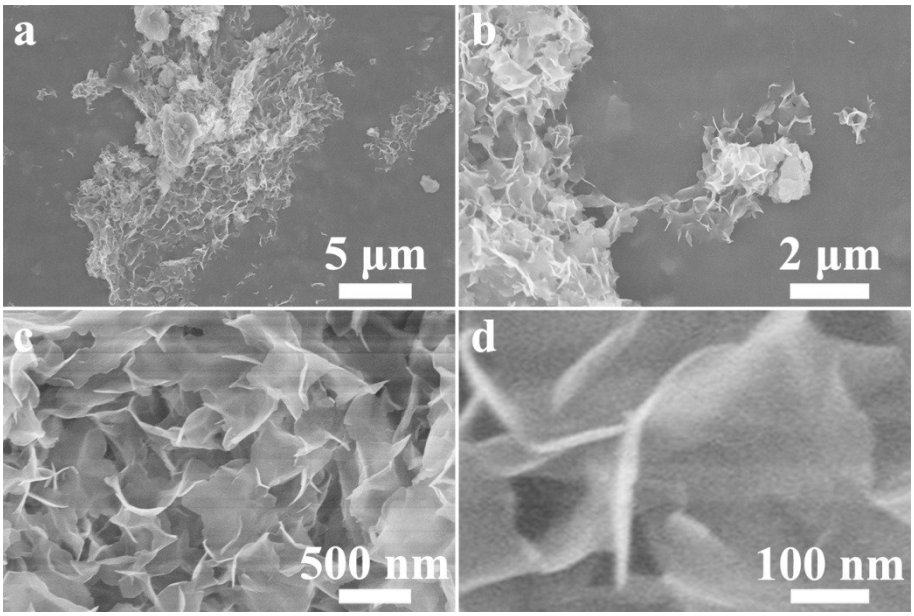

Figure S4. SEM images of LDH with different magnifications.

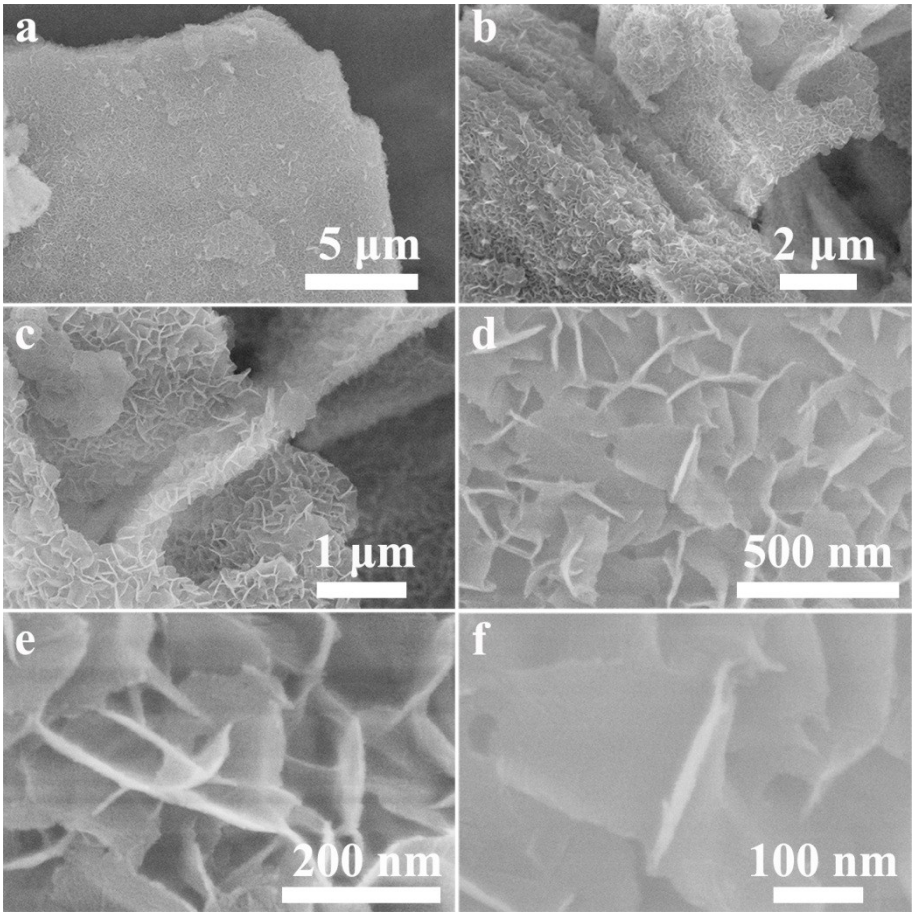

Figure S5. SEM images of rGO@LDH with different magnifications.

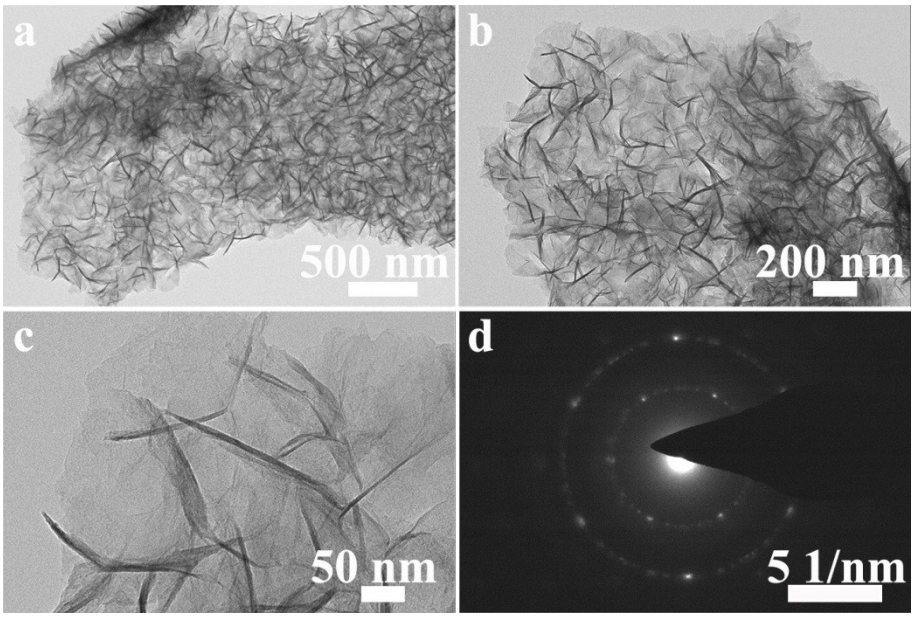

Figure S6. TEM images of rGO@LDH with different magnifications (a,b,c) and (d) the SAED pattern of rGO@LDH.

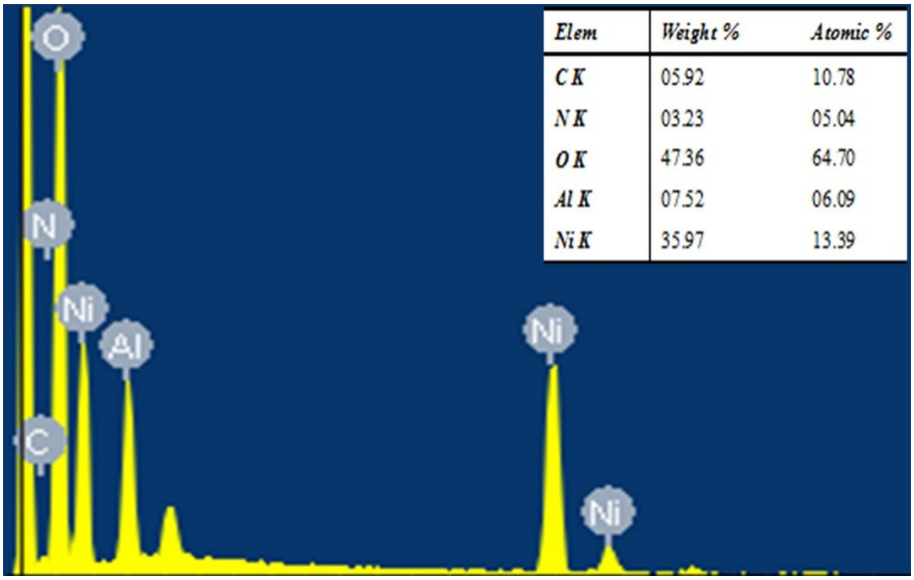

Elem	Weight %	Atomic %
C K	05.92	10.78
N K	03.23	05.04
O K	47.36	64.70
Al K	07.52	06.09
Ni K	35.97	13.39

Figure S7. EDX spectrum of GP@LDH. The inserted table summarizes the weight and atomic ratios of elements in GP@LDH.

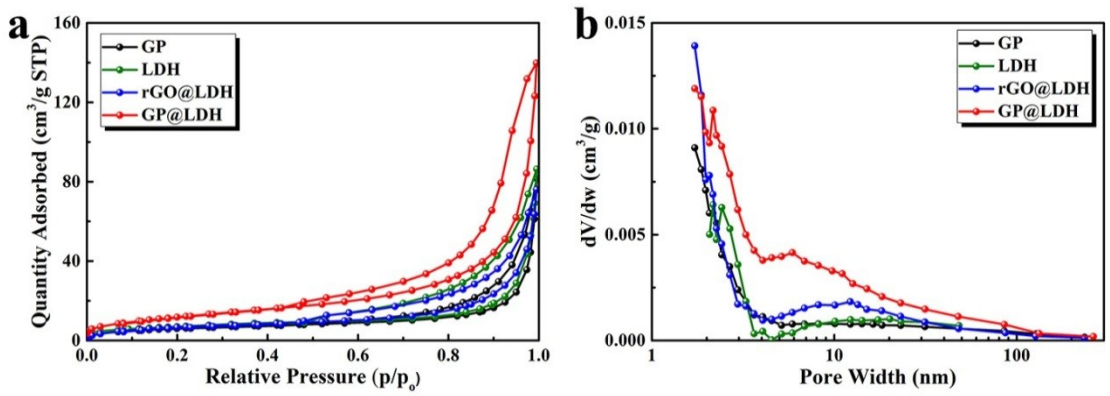

Figure S8. (a) N_2 adsorption/desorption isotherms of GP, LDH, rGO@LDH and GP@LDH; (b) Pore-size distributions of GP, LDH, rGO@LDH and GP@LDH.

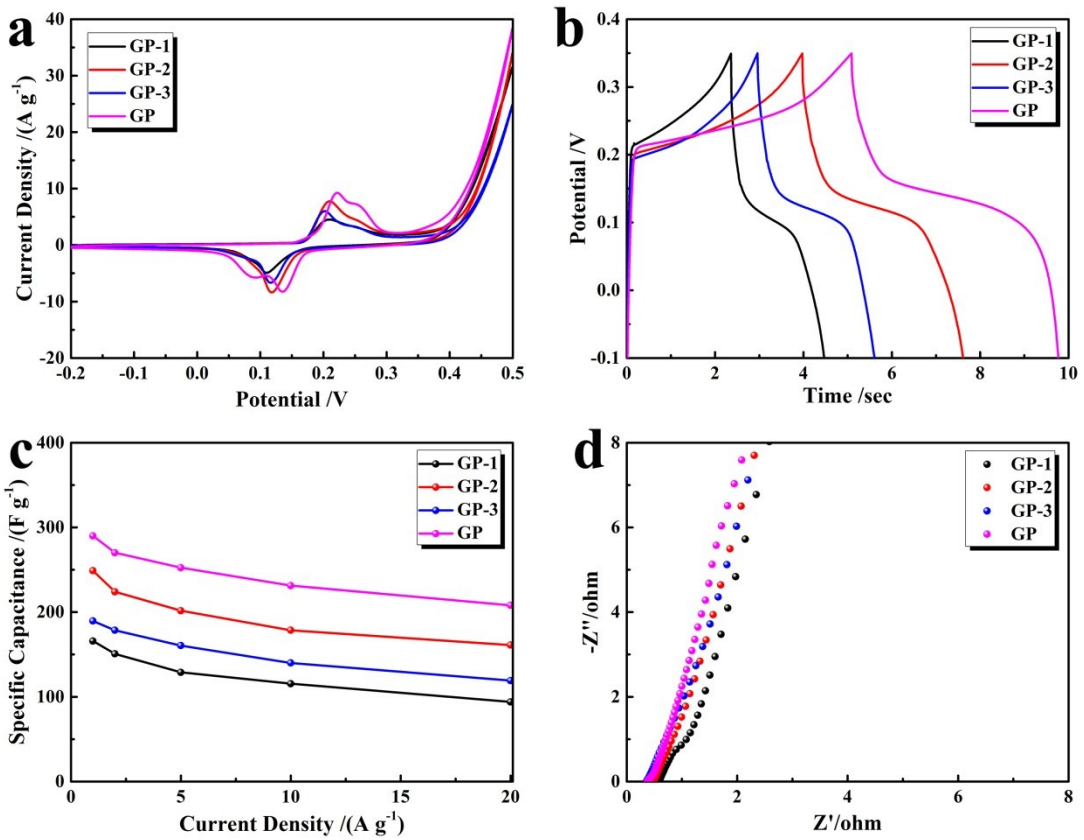

Figure S9. Comparison of capacitive performance for the GP samples with different thickness of polypyrrole.

Comparing the CV curves of four GP samples, the CV curve of GP with a thickness of 43 nm has a maximal area surrounded (**Figure S9a**), indicating the best capacitive performance, which could be directly observed in **Figure S9b**. Besides, GCD tests also show that the specific capacitances of GP are higher than the other three samples at all current densities from 1 A g^{-1} to 20 A g^{-1} (**Figure S9c**). Additionally, Nyquist plots also indicate the relatively small charge transfer resistance at the electrode and electrolyte interface and the best capacitive behavior of the samples (**Figure S9d**). Above analyses demonstrated that the GP with a thickness of 43 nm has the optimized capacitive performance.

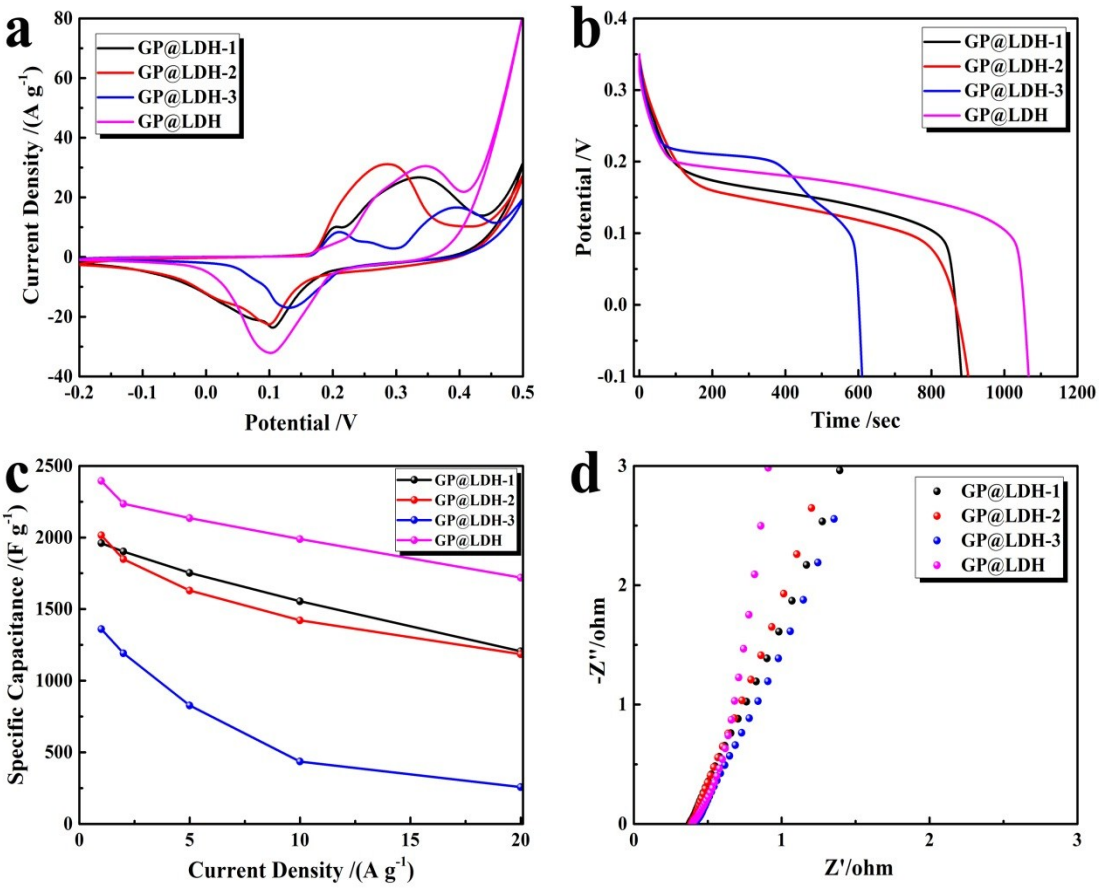

Figure S10. (a) Cyclic voltammograms at a scan rate of 5 mV s^{-1}; (b) Galvanostatic charge-discharge curves at a current density of 20 A g^{-1}; (c) The variation in the specific capacitance as a function of current density; (d) Nyquist plots of GP@LDH-1, GP@LDH-2, GP@LDH-3 and GP@LDH.

In the four GP@LDHs samples, the GP@LDH has the best kinetic reversibility (**Figure S10a**) and the largest specific capacitance at a large current density of 20 A g^{-1} (**Figure S10b**). Moreover, the rate performance and Nyquist plots of the four samples were also exhibited in **Figure S10c** and **Figure S10d**, respectively. It can be clearly seen that the specific capacitance of GP@LDH are higher than the other three samples at all current densities from 1 A g^{-1} to 20 A g^{-1} (**Figure S10c**). And the Nyquist plots demonstrate very small electron/ion transfer resistance and very good capacitive

behavior of these samples (**Figure S10d**). Above analyses show that the GP@LDH has the optimized capacitive performance among these four samples.

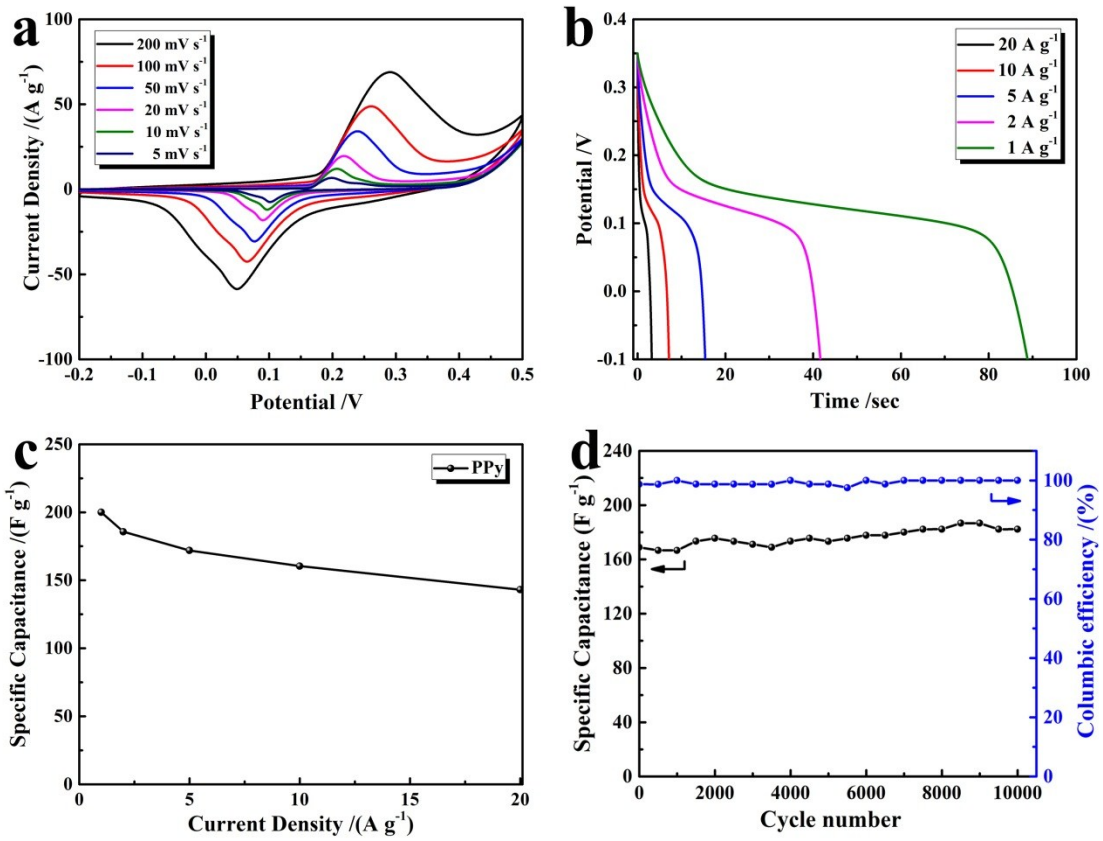

Figure S11. (a) Cyclic voltammograms of PPy at various scan rates; (b) Galvanostatic charge-discharge curves of PPy at current densities of 1, 2, 5, 10 and 20 A g^{-1}; (c) The variation in the specific capacitance of PPy as a function of current density; (d) The cycle life of PPy at the current density of 10 A g^{-1} and the corresponding columbic efficiency in a 6 M KOH solution.

It can be seen that the CV curves (**Figure S11a**) at the scan rates of 5 to 200 mV s^{-1} possess essentially similar shape and relatively symmetric redox peaks, demonstrating a good kinetic reversibility for PPy. As calculated by the discharge branch of GCD curves (**Figure S11b**), the specific capacitances of pure PPy reach 200, 186, 172, 160 and 143 F g^{-1} when the current density is 1, 2, 5, 10 and 20 A g^{-1}, respectively (**Figure S11c**). The specific capacitance values are much lower than GP@LDH, although PPy (**Figure S11d**) does contribute to the overall capacitance of GP@LDH. More

importantly, the exceptive cycling stability of PPy ensures that GP@LDH has a structural integrity during reduplicative charge/discharge processes.

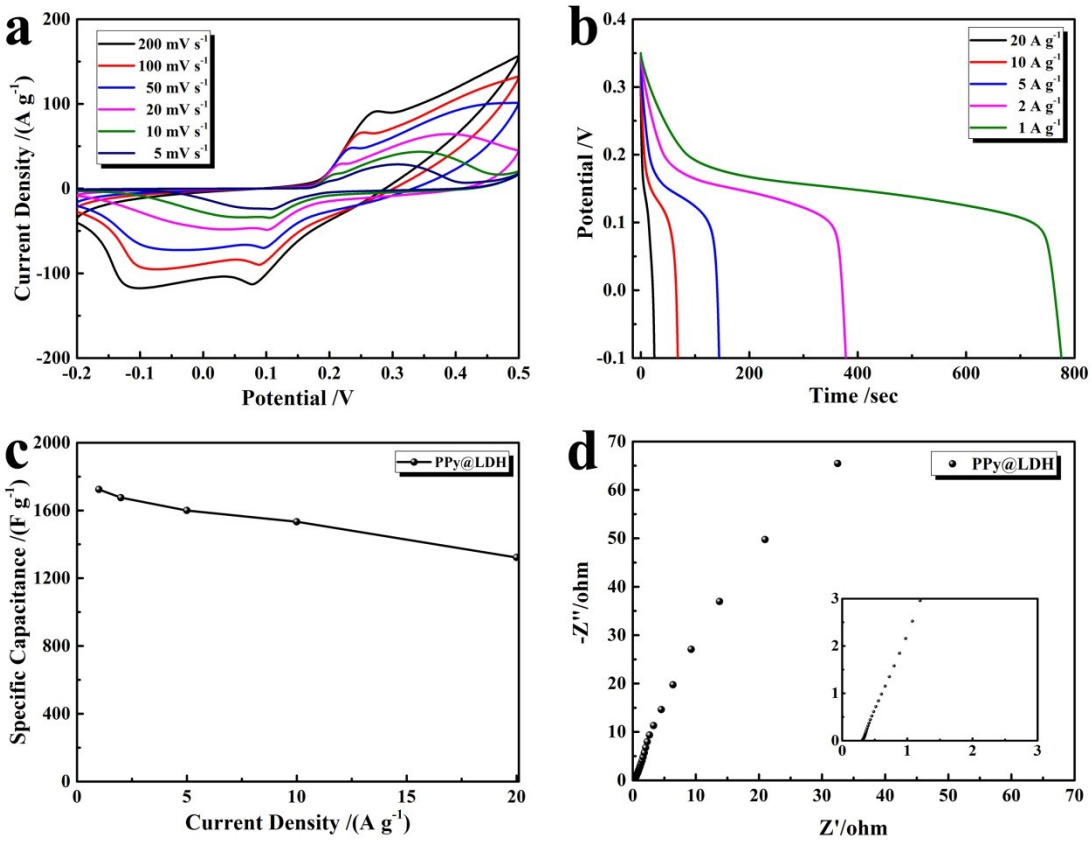

Figure S12. (a) Cyclic voltammograms of PPy@LDH at various scan rates; (b) Galvanostatic charge-discharge curves of PPy@LDH at current densities of 1, 2, 5, 10 and 20 A g^{-1}; (c) The variation in the specific capacitance of PPy@LDH as a function of current density; (d) Nyquist plot of PPy@LDH (the inset is enlarged Nyquist plot).

The capacitive performance of PPy was intensively studied by CV and GCD analyses (**Figure S12**). It can be seen that the CV curves (**Figure S12a**) at the scan rates of 5 to 200 mV s^{-1} possess essentially similar shape and relatively symmetric redox peaks, and the CV curve of PPy@LDH has a maximal area surrounded (**Figure S12a**), indicating the largest specific capacitance. As calculated by the discharge branch of GCD curves (**Figure 3, S12b**), PPy@LDH has a highly improved specific capacitance (1723.73 F g^{-1} at 1 A g^{-1}) and enhanced rate performance (retaining 76.73% of its initial capacitance at the current density of 20 A g^{-1}) if compared to pure LDH (**Figure 3**) with lower

specific capacitance (762.57 F g^{-1} at 1 A g^{-1}) and inferior rate performance (retaining 17.54% of its initial capacitance). Besides, owing to the conductive PPy added, PPy@LDH (**Figure S12d**) also exhibited lower ion diffusion and charge transfer resistances than those of pure LDH (**Figure 3f**). These prominently enhanced capacitive performance indicated the existence of synergetic effect between PPy and LDH.

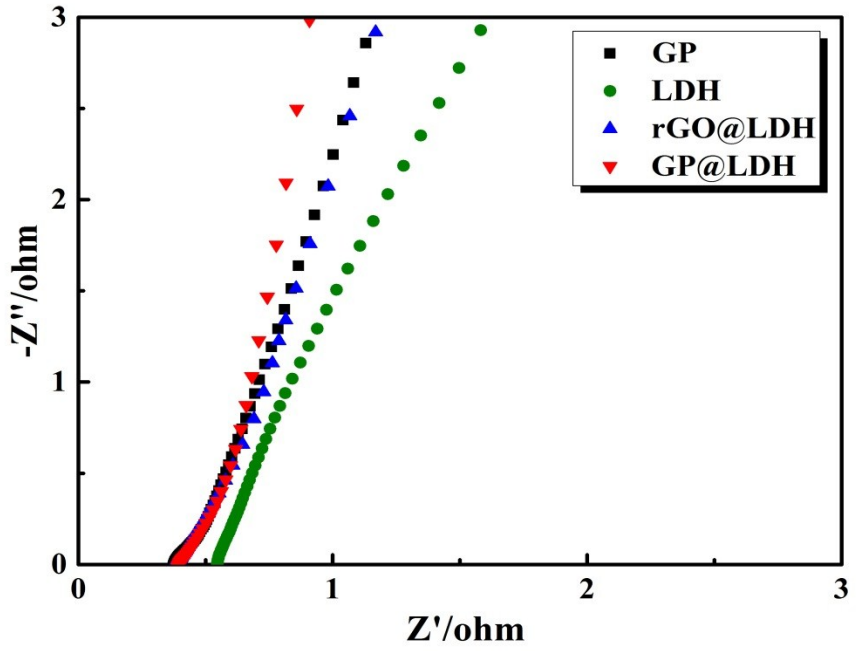

Figure S13. Enlarged Nyquist plots of GP, LDH, rGO@LDH and GP@LDH.

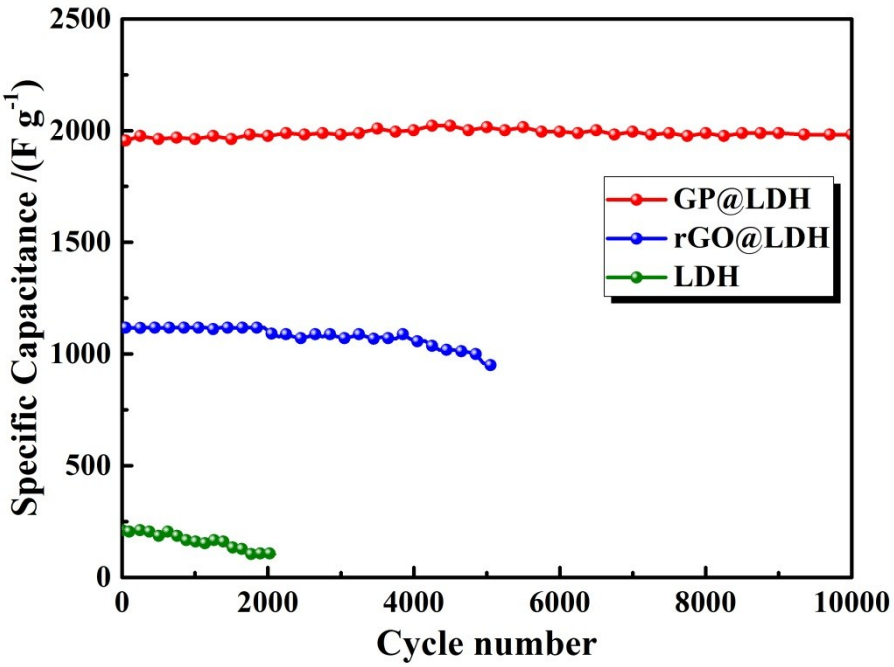

Figure S14. A plot of specific capacitance vs. cycle number for GP@LDH, rGO@LDH and LDH at the current density of 10 A g^{-1}.

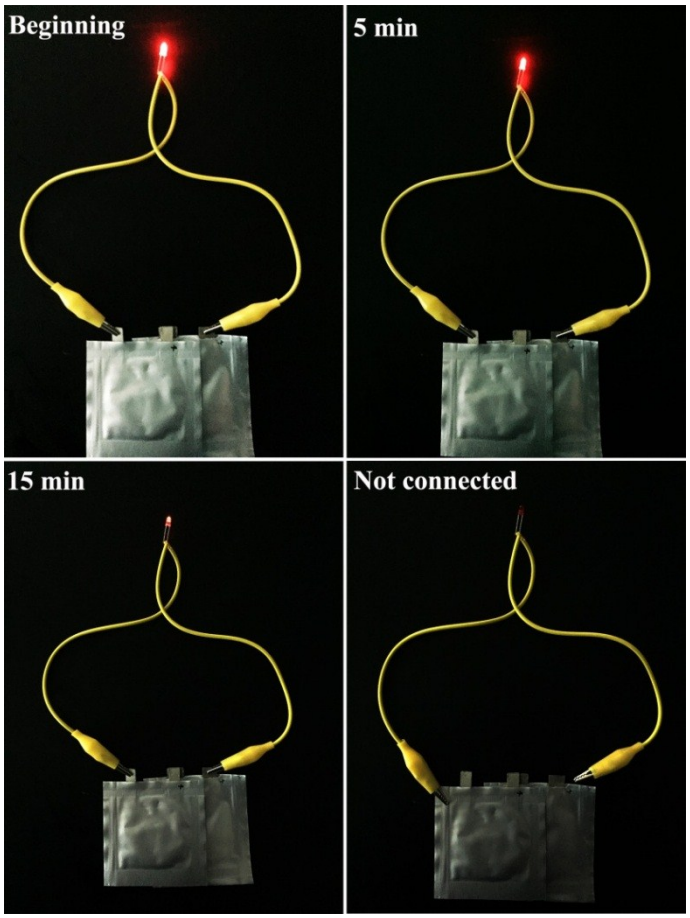

Figure S15. Digital photos of lighted LED at different discharge times.

Table S1. Surface area and pore structure parameters of the as-prepared samples

Samples	S_{BET}[a]	S_{Micro}[b]	S_{Meso}[c]	V_{Total}[d]	V_{Meso}[e]	D[f]
	m^2g^{-1}	m^2g^{-1}	m^2g^{-1}	cm^3g^{-1}	cm^3g^{-1}	nm
GP	21	4	17	0.13	0.05	24.76
LDH	25	5	20	0.13	0.06	20.80
rGO@LDH	24	3	21	0.12	0.07	20.00
GP@LDH	44	2	42	0.23	0.13	20.91

[a] BET surface area. [b] Micropore surface area calculated by t-plot method. [c] Mesopore surface area equal to S_{BET} minus S_{Micro}. [d] Total pore volume measured at a relative pressure (P/P_o) of 0.99. [e] The BJH mesopore volume. [f] The average pore size calculated by $4V_{Total}/S_{BET}$.

Table S2. Comparison of the capacitive performance of GP@LDH with similar electrode materials reported in the literatures.

Materials	**Capacitance (F/g)**	**Rate capability**	**Ref.**
GP@LDH	2395 (1 A/g)	71.8% (20 A/g)	**This work**
Co–Al LDH	1075 (5 mA/cm^2)	72% (50 mA/cm^2)	2
Ni-Co-Al-LDH	1289 (1 A/g)	57% (30 A/g)	3
Ni–Co LDH	1000 (5 mv/s)	69% (500 mv/s)	4
$Co(OH)_2$	1116 (2 A/g)	38% (10 A/g)	5
Ni–Co–Al LDH/RGO/CNT	1188 (1 A/g)	72% (10 A/g)	6
Co–Al LDH/graphene	712 (1 A/g)	73% (10 A/g)	7
GSP-LDH	1043 (1 A/g)	87% (20 A/g)	8
NiCo LDH/CNT	1843 (0.5 A/g)	66.7% (10 A/g)	9
NiMn LDHGOS	2246.63 (1 A/g)	74.3% (10 A/g)	10
Fe_3O_4@C@NiAl LDH	767.6 (1 A/g)	52.8% (10 A/g)	11
CoAl-LDH	584 (1 A/g)	39% (40 A/g)	12
MoS_2@$Ni(OH)_2$	516 (2 A/g)	48% (10 A/g)	13
MnOOH@NiO	1890 (2 A/g)	64% (20 A/g)	14
$NiCo_2O_4$	1045 (5 A/g)	56% (20 A/g)	15
H-OH-LDH	1031 (1 A/g)	74% (40 A/g)	16

Table S3. Comparison of capacitive performance between GP@LDH//AGP and similar asymmetric supercapacitors recently reported.

Electrode materials	**Potential range (V)**	**Energy density (Wh kg^{-1})**	**Power density (W kg^{-1})**	**Ref.**
GP@LDH//AGP	1.6	94.4	463.1	**This work**
Ni_xCo_{1-x}LDHs//AC	1.2	23.7	284.2	17
$NiCo_2O_4$@$Co_{0.33}Ni_{0.67}(OH)_2$//CMK-3	1.6	31.2	396	18
$Co_{0.45}Ni_{0.55}O$-RGO//RGO	1.5	35.3	330	19
$NiCo_2O_4$-rGO//AC	1.3	23.32	324.9	20
Ni,Co-OH/rGO//HPC	1.6	56.1	76	21
NiAl LDH@CNPs//AC	1.6	47.7	1500	22
Ni-Co LDH//AC	1.5	17.5	10500	23
NiCo-LDHs@CNT/NF//APDC/NF	1.8	89.7	456.8	24
CoAl LDH/ACT//ACT/graphene	1.6	55.04	387.9	25
CoMn LDH/Ni foam//AC	1.8	4.4	2500	26
CBC-N_2@LDH-0.4//CBC-N_2	1.6	36.3	800	27

Reference

1 Z. Weng, F. Li, D. W. Wang, L. Wen and H. M. Cheng, *Angewandte Chemie International Edition*, 2013, **52**, 3722–3725.

2 L. Z, Z. W, L. X, W. GR, O. H. D, C. Z, S. X and D. X, *Nanoscale*, 2012, **4**, 3640-3643.

3 J. Yang, C. Yu, X. Fan and J. Qiu, *Advanced Energy Materials*, 2014, **4**.

4 J. C. Chen, C. T. Hsu and C. C. Hu, *Journal of Power Sources*, 2014, **253**, 205-213.

5 R. R. Salunkhe, B. P. Bastakoti, C. T. Hsu, N. Suzuki, J. H. Kim, S. X. Dou, C. C. Hu and Y. Yamauchi, *Chemistry - A European Journal*, 2014, **20**, 3084-3088.

6 C. Yu, J. Yang, C. Zhao, X. Fan, G. Wang and J. Qiu, *Nanoscale*, 2013, **6**, 3097-3104.

7 L. Zhang, X. Zhang, L. Shen, B. Gao, L. Hao, X. Lu, F. Zhang, B. Ding and C. Yuan, *Journal of Power Sources*, 2011, **199**, 395-401.

8. X. Wu, L. Jiang, C. Long, T. Wei and Z. Fan, *Advanced Functional Materials*, 2015, **25**, 1648–1655.

9 H. Chen, F. Cai, Y. Kang, S. Zeng, M. Chen and Q. Li, *ACS Applied Materials & Interfaces*, 2014, **6**, 19630-19637.

10 J. Chen, X. Wang, J. Wang and P. S. Lee, *Advanced Energy Materials*, 2016, **6**.

11 L. Li, R. Li, S. Gai, F. He and P. Yang, *Journal of Materials Chemistry A*, 2014, **2**, 8758-8765.

12 J. Han, Y. Dou, J. Zhao, M. Wei, D. G. Evans and X. Duan, *Small*, 2013, **9**, 98–106.

13 G. Wang, H. Wang, X. Lu, Y. Ling, M. Yu, T. Zhai, Y. Tong and Y. Li, *Advanced Materials*, 2014, **26**, 2676-2682.

14 J. Sun, W. Li, B. Zhang, G. Li, L. Jiang, Z. Chen, R. Zou and J. Hu, *Nano Energy*, 2014, **4**, 56-64.

15 J. Zhu, Z. Xu and B. Lu, *Nano Energy*, 2014, **7**, 114-123.

16 X. Liu, A. Zhou, T. Pan, Y. Dou, M. Shao, J. Han and M. Wei, *Journal of Materials Chemistry A*, 2016, **4**, 8421-8427.

17 X. Wang, A. Sumboja, M. Lin, J. Yan and P. S. Lee, *Nanoscale*, 2012, **4**, 7266-7272.

18 K. Xu, R. Zou, W. Li, Q. Liu, X. Liu, L. An and J. Hu, *Journal of Materials Chemistry A*, 2014, **2**, 10090-10097.

19 J. Xiao, *Journal of Materials Chemistry*, 2012, **22**, 12253-12262.

20 X. Wang, W. S. Liu, X. Lu and P. S. Lee, *Journal of Materials Chemistry*, 2012, **22**, 23114-23119.

21 H. Ma, J. He, D. B. Xiong, J. Wu, Q. Li, V. Dravid and Y. Zhao, *ACS Applied Materials & Interfaces*, 2016, **8**.

22 X. Liu, C. Wang, Y. Dou, A. Zhou, T. Pan, J. Han and M. Wei, *Journal of Materials Chemistry A*, 2014, **2**, 1682-1685.

23 M. Jing, H. Hou, C. E. Banks, Y. Yang, Y. Zhang and X. Ji, *ACS Applied Materials & Interfaces*, 2015, **7**.

24 X. Li, J. Shen, W. Sun, R. T. Wang, X. Hong, X. Zhao and X. Yan, *Journal of Materials Chemistry A*, 2015, **3**, 13244-13253.

25 Z. Gao, C. Bumgardner, N. Song, Y. Zhang, J. Li and X. Li, *Nature Communications*, 2016, **7**.

26 A. D. Jagadale, G. Guan, X. Li, X. Du, X. Ma, X. Hao and A. Abudula, *Journal of Power Sources*, 2016, **306**, 526-534.

27 F. Lai, Y. E. Miao, L. Zuo, H. Lu, Y. Huang and T. Liu, *Small*, 2016, **12**, 3199-3199.